

Long mmWave Backhaul Connectivity Using Fixed-Wing UAVs

Mohammad T. Dabiri, Mazen. O. Hasna, Nizar Zorba, and Tamer Khattab

Department of Electrical Engineering, Qatar University, Doha, Qatar,

E-mails: (m.dabiri@qu.edu.qa; hasna@qu.edu.qa; nizarz@qu.edu.qa;

tkhattab@qu.edu.qa).

Abstract

This paper discusses the analysis of a fixed wing unmanned aerial vehicle (UAV)-based millimeter wave (mmWave) backhaul link, that is offered as a cost effective and easy to deploy solution to connect a disaster or remote area to the nearest core network. We present the optimal design of a relay system based on fixed wing UAV, taking into account the actual channel parameters such as the UAV vibrations, tracking error, real 3GPP antenna pattern, UAV's height, flight path, and the effect of physical obstacles. The performance of the considered system is evaluated in terms of outage probability and the channel capacity, while taking into account the impact of the system parameters such as optimal selection of UAV flight path and antenna patterns

Index Terms

Antenna pattern, backhaul/frounhaul links, positioning, mmWave communication, unmanned aerial vehicles (UAVs).

I. INTRODUCTION

Natural disaster comprising earthquakes, hurricanes, tornadoes, floods, and other geologic processes can potentially cut or entirely destroy wired communications (e.g. fiber) infrastructure to the disaster area. Any disruption to the fragile fiber causes data disconnections that take days to find and repair. However, providing an alternative wireless connection link in the immediate moments after a disaster event is an essential need to facilitate rescue operations, as well as

This publication was made possible by NPRP13S-0130-200200 from the Qatar National Research Fund (a member of The Qatar Foundation). The statements made herein are solely the responsibility of the author[s].

to provide internet connectivity to the people escaping from the affected area. Providing an alternative terrestrial wireless backhaul connectivity encounters serious challenges, including creating a line of sight (LoS) between the disaster area to the nearest connected core network, especially in forest and mountainous areas. Due to their unique capabilities such as flexibility, maneuverability, and adaptive altitude adjustment, unmanned aerial vehicles (UAVs) acting as networked flying platforms (NFPs) can be considered as a promising solution to provide a temporary wireless backhaul connectivity while improving reliability of backhaul operations [1], [2]. More recently, millimeter wave (mmWave) backhauling has been proposed as a promising approach for aerial communications because of three reasons [3]. First, unlike terrestrial mmWave communication links that suffer from blockage, the flying nature of UAVs offers a higher probability of LoS between communication nodes. Second, the large available bandwidth at mmWave frequencies can provide high data rate point-to-point aerial communication links, as needed for the backhaul communications. Third, to compensate the negative effects of the high path-loss at the mmWave bands, the small wavelength enables the realization of a compact form of highly directive antenna arrays, which is suitable for small UAVs with limited payload. Although NFP-based mmWave backhaul link has been studied in recent works [3]–[13], the results of these studies are limited for rotary-wing UAVs.

Rotary wing UAVs are used in cases where more maneuverability is required, for example, to provide internet service in crowded urban areas. To keep the rotary wing UAV stable in the air, its motors are required to individually speed up or slow down its propellers, which can be time consuming, mainly due to UAV inertia. Moreover, scaling the rotary-wing UAV up to a larger size faces major challenges because more energy is needed to change speed of larger propellers. Another set of challenges for rotary-wing UAVs stems from restrictions on payload, altitude, and shorter flight times. Being able to fly for longer times, at higher altitudes, and with heavier payloads than rotary-wing UAVs are the greatest advantages of fixed wing UAVs. All these characteristics make them suitable for remote or disaster area applications. Based on the results of [3], [12], to design an aerial mmWave backhaul link based on a rotary wing UAV, the goal is to find an optimal point in 3D space relative to the ground transmitter and receiver. However, fixed wing UAVs cannot hover or make sharp turns, and thus, the results of the aforementioned works are not directly applicable for fixed wing UAVs.

In this study, we consider a mmWave backhaul link based on fixed wing UAV, as shown in Fig. 1, that is offered as a cost effective and easy to deploy solution to connect a disaster or remote

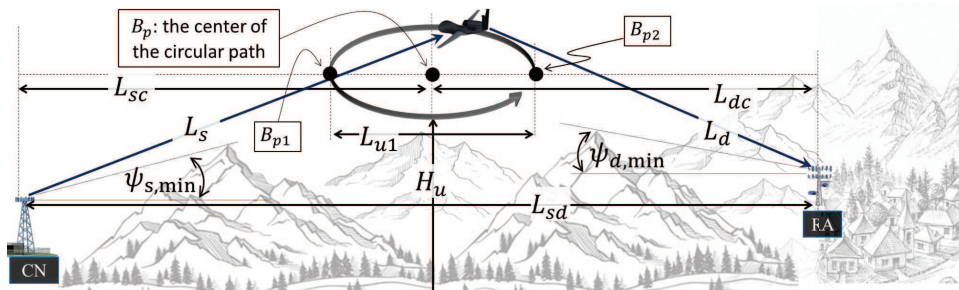


Fig. 1. A fixed wing UAV acting as an NFP node in order to relay data from the nearest core network to the disaster or remote area.

area to the nearest core network in a short time. We fully characterize the scenario by taking into account the effects of realistic physical parameters, such as the UAV's circular path, critical points of the flight path, heights and positions of obstacles, flight altitude, tracking errors, the severity of UAV's vibrations, the real 3D antenna pattern provided by 3GPP, atmospheric channel loss, temperature and air pressure. We evaluate the performance of the considered system in two terms: outage probability and the average (ergodic) channel capacity. We identify the critical points on the UAV's flight path and design the flight path of the UAV in such a way that guarantees the requested quality of service (QoS) at the considered critical points. Then, in the next step, by choosing the optimal antenna pattern, we try to maximize the capacity of the considered system.

The rest of this paper is organized as follows. We introduce the channel model of a rotary wing UAV-based mmWave backhaul link in Section II. Our optimization problem along with the performance of the considered system, in terms of the channel capacity and the outage probability are characterized in Section III. Using the simulation results, we study the optimal parameter design of the considered system, in Section IV. Finally, conclusions and future road map are drawn in Section V.

II. SYSTEM MODEL

We consider a fixed wing UAV acting as an NFP node in order to relay data from the nearest core network (CN) to the disaster or remote area (RA). The fixed-wing UAV rotates in a circular path with center B_p and diameter L_{u1} as depicted in Fig. 1. Point B_{p1} shown in Fig. 1 is the closest and farthest point to the CN and RA, respectively. On the other hand, B_{p2} is the farthest

TABLE I
THE LIST OF MAIN NOTATIONS.

Parameter	Description
$v \in \{t, r\}$	This subscript is used to specify Tx and Rx antennas
$q \in \{s, d\}$	This subscript is used to specify A_s and A_d
$w \in \{x, y\}$	This subscript is used to specify x and y axes
A_{us}	The NFP antenna directed toward the A_s
A_{ud}	The NFP antenna directed toward the A_d
A_s	Antenna of CN
A_d	Antenna of RA
$P_{t,s}$	Transmitted power of A_s
$P_{t,d}$	Transmitted power of A_{ut}
N_{uqw}	Number of antenna elements of A_{uq} in w axis
N_{qw}	Number of antenna elements of A_q in w_q axis
θ_{qw}	Instantaneous misalignment of A_q in $w_q - z_q$ plane
θ_{uqw}	Instantaneous misalignment of A_{uv} in $w_q - z_q$ plane
μ_{qw}	Mean of RV θ_{qw}
σ_{qw}^2	Variance of RV θ_{qw}
μ_{uqw}	Mean of RV θ_{uqw}
σ_{uqw}^2	Variance of RV θ_{uqw}
λ and f_c	Wavelength and carrier frequency, respectively
B_{p1}	The farthest and closest point to A_d and A_s
B_{p2}	The farthest and closest point to A_s and A_d
B_p	The center of UAV circular path
$\psi_{q,\min}$	Minimum elevation angle
H_u	Heights of NFP
L_q	Link length of A_q to NFP
L_{sd}	Horizontal distance between A_s and A_d
L_{qc}	Horizontal distance between A_q and point B_p

and closest point to the CN and RA, respectively. Let $\psi_{s,\min}$ and $\psi_{d,\min}$ denote the minimum elevation angles of CN and RA, respectively, L_s represents the link length from CN to UAV (CU), L_d denotes the link length between UAV to RA (UR), L_{sd} shows the distance between CN to RA, and H_u stands for the UAV height.

As shown in Fig. 2, our topology consists of four mmWave array antennas. We consider that z_s represents the propagation axis of CU link and axes x_s and y_s represent the array antenna

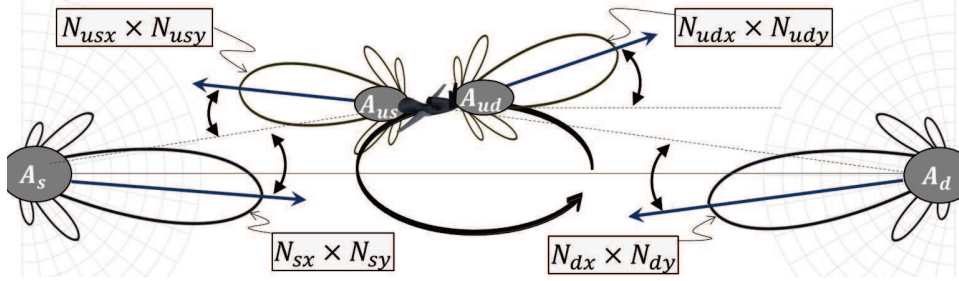


Fig. 2. A graphical illustration of antenna pattern misalignment.

plane perpendicular to the propagation axis. Similarly, z_d axis represents the propagation axis of UR link, while axes x_d and y_d represent the array antenna plane perpendicular to the propagation axis z_d . Let $A_s(N_{sx} \times N_{sy})$ denotes the CN array antenna composed of $N_{sx} \times N_{sy}$ elements, where N_{sx} and N_{sy} are the number of antenna elements in the x_s axis and y_s axis directions, respectively, within the $x_s - y_s$ plane. Similarly, let $A_d(N_{dx} \times N_{dy})$ denotes the array antenna of RA node, $A_{us}(N_{usx} \times N_{usy})$ denotes the array antenna of the NFP directed toward the CN, and $A_{ud}(N_{udx} \times N_{udy})$ denotes the array antenna of NFP directed toward the RA, respectively. Antennas A_s and A_{us} as well as antennas A_d and A_{ud} try to adjust the direction of their antennas to each other. At first, it may seem that by increasing the number of antenna elements, which leads to an increase in antenna gain, the system performance improves. However, in practical situations, increasing the antenna gain makes the system more sensitive to antenna misalignment. A change in the instantaneous speed and acceleration of the fixed wing UAV, an error in the mechanical control system of UAV, mechanical noise, position estimation errors, air pressure, and wind speed can cause an alignment error between the antennas [14], as graphically illustrated in Fig. 2. Therefore, the optimal design of the antenna patterns is of great importance in the presence of alignment error. Let $\theta_{qw} \sim \mathcal{N}(\mu_{qw}, \sigma_{qw}^2)$ be the instantaneous random misalignment angle of A_q in $w_q - z_q$ plane, where $q \in \{s, d\}$ and $w \in \{x, y\}$. Similarly, $\theta_{uqw} \sim \mathcal{N}(\mu_{uqw}, \sigma_{uqw}^2)$ be the instantaneous random misalignment of A_{uq} in $w_q - z_q$ plane.

1) *Channel Propagation Loss*: In normal atmospheric conditions, water vapor (H_2O) and oxygen (O_2) molecules are strongly absorptive of radio signals, especially at mmWave frequencies and higher. The resulting attenuation is in excess of the reduction in radiated signal power due

to free-space loss. Channel loss (in dB) is usually expressed as

$$h_{L,\text{dB}}^{\text{tot}}(f_c) = 20 \log \left(\frac{4\pi L}{\lambda} \right) + h_{L,\text{dB}}^{o,w}(f_c), \quad (1)$$

where L is the link length (in m), λ is the wavelength (in m), f_c is mmWave frequency (in GHz), $h_{L,\text{dB}}^{o,w}(f_c) = \frac{h_{L,\text{dB/km}}^{o,w}(f_c)L}{1000}$ is the attenuation due to oxygen and water (in dB), $h_{L,\text{dB/km}}^{o,w}(f_c) = h_{L,\text{dB/km}}^o(f_c) + h_{L,\text{dB/km}}^w(f_c)$ is the attenuation due to oxygen and water (in dB/km). At 20°C surface temperature and at sea level, approximate expressions for the attenuation constants of oxygen and water vapor (in dB/km) as defined by the International Telecommunications Union (ITU) are [15]:

$$h_{L,\text{dB/km}}^{o,0}(f_c) = 0.001 \times f_c^2 \quad (2)$$

$$\times \begin{cases} \frac{6.09}{f_c^2 + 0.227} + \frac{4.81}{(f_c - 57)^2 + 1.5} & f_c < 57 \\ h_{L,\text{dB/km}}^{o,0}(f_c = 57) + 1.5(f_c - 57) & 57 < f_c < 63 \\ \frac{4.13}{(f_c - 63)^2 + 1.1} + \frac{0.19}{(f_c - 118.7)^2 + 2} & 63 < f_c < 350 \end{cases}$$

and

$$h_{L,\text{dB/km}}^{w,0}(f_c) = 0.0001 \times f_c^2 \rho_0 \left(0.05 + \frac{3.6}{(f_c - 22.2)^2 + 8.5} + \frac{10.6}{(f_c - 183.3)^2 + 9} + \frac{8.9}{(f_c - 325.4)^2 + 26.3} \right), \quad f_c < 350, \quad (3)$$

where $\rho_0 = 7.5 \text{ g/m}^3$ is the water vapor density at sea level, and $h_{L,\text{dB/km}}^{o,0}(f_c = 57)$ is the value of the first expression at $f_c = 57$. In general, the attenuation constants of oxygen and water vapor are functions of altitude, since they depend on factors such as temperature and pressure. These quantities are often assumed to vary exponentially with height H , as $\rho(H) = \rho_0 \exp(-H/H_{\text{scale}})$ where H_{scale} is known as the scale height, which is typically 1-2 km. From this, the specific attenuation as a function of height can be approximately modeled as

$$h_{L,\text{dB/km}}^{o,w}(f_c, H) = h_{L,\text{dB/km}}^{o,w,0}(f_c) \exp(-H/H_{\text{scale}}). \quad (4)$$

In our system model, both CU and UR links are slant. For a slant atmospheric path from height H_1 to H_2 at an angle ψ , the total atmospheric attenuation is obtained by integration from (4) as

$$h_{L,\text{dB/km}}^{o,w}(f_c) \simeq \frac{h_{L,\text{dB/km}}^{o,w,0}(f_c) (e^{-H_1/H_{\text{scale}}} - e^{-H_2/H_{\text{scale}}}) H_s}{\sin(\psi)}. \quad (5)$$

III. PERFORMANCE ANALYSIS

For a given region with physical parameters such as air pressure, temperature, $\psi_{s,\min}$, $\psi_{d,\min}$, and H_{sd} , our aim is to adjust the tunable system parameters such as N_{sx} , N_{sy} , N_{dx} , N_{dy} , N_{usx} , N_{usy} , N_{udx} , N_{udy} , H_u and L_{sc} , to improve system performance in terms of average capacity and the outage probability. These two metrics are very important in the design of wireless communication systems. Our objective is to maximize the channel capacity with the outage probability as a constraint (it is less than a threshold, i.e., $\mathbb{P}_{\text{out}} < \mathbb{P}_{\text{out,th}}$, where $\mathbb{P}_{\text{out,th}}$ is determined based on the requested quality of service (QoS)). Our optimization problem is formulated as:

$$\max_{\substack{N_{sx}, N_{sy}, N_{dx}, N_{dy}, \\ N_{usx}, N_{usy}, N_{udx}, N_{udy}, \\ H_u, L_{su}}} \bar{\mathbb{C}}_{e2e} \quad (6a)$$

$$\text{s.t.} \quad \mathbb{P}_{\text{out}} < \mathbb{P}_{\text{out,tr}} \quad (6b)$$

$$H_u > H_{u,\min}, \quad (6c)$$

where $\bar{\mathbb{C}}_{e2e}$ is the average channel capacity during the UAV flight time. Constraint (6c) is used in order to guarantee the UAV be in the LoS of both CN and RA throughout the entire flight path. Therefore, the minimum height of the UAV should be

$$H_{u,\min} = \max \left\{ \left(L_{sc} + \frac{L_{u1}}{2} \right) \sin(\psi_{s,\min}), \left(L_{dc} + \frac{L_{u1}}{2} \right) \sin(\psi_{d,\min}) \right\}, \quad (7)$$

to ensure it satisfies the LoS for both links. In (7), we have $L_{sc} = \sqrt{L_{s,\min}^2 - H_u^2} + \frac{L_{u1}}{2}$, $L_{dc} = \sqrt{L_{d,\min}^2 - H_u^2} + \frac{L_{u1}}{2}$, where $L_{s,\min}$ is the link length between CN and B_{p1} , while $L_{d,\min}$ is the link length between RA to B_{p2} . We consider that the points B_p , B_{p1} , and B_{p2} are in $[x, y] = [0, 0]$, $[\frac{L_{u1}}{2}, 0]$, and $[-\frac{L_{u1}}{2}, 0]$, respectively. Let \mathcal{R}_1 indicate the path of a semicircle that starts from point B_{p1} and reaches point B_{p2} . Therefore, each point on \mathcal{R}_1 in the $[x - y]$ plane is specified as follows

$$x_u = \frac{L_{u1}}{2} \cos(\theta_{R1}), \quad y_u = \frac{L_{u1}}{2} \sin(\theta_{R1}), \quad (8)$$

where $0 < \theta_{R1} < \pi$. From this, the average channel capacity can be formulated as

$$\bar{\mathbb{C}}_{e2e} = \frac{1}{\pi} \int_{\theta_{R1}=0}^{\pi} \min \{ \mathbb{C}_{su}(\theta_{R1}), \mathbb{C}_{du}(\theta_{R1}) \} d\theta_{R1}, \quad (9)$$

where $\mathbb{C}_{su}(\theta_{R1})$ and $\mathbb{C}_{du}(\theta_{R1})$ are the average channel capacities of SU and UR links conditioned on θ_{R1} , respectively. For our system model, $\mathbb{C}_{qu}(\theta_{R1})$ is a function of random variables (RVs) θ_{qx} , θ_{qy} , θ_{uqx} , and θ_{uqy} and can be obtained as

$$\begin{aligned} \mathbb{C}_{qu}(\theta_{R1}) &= \frac{1}{4\pi^2\sigma_{qx}\sigma_{qy}\sigma_{rqx}\sigma_{rqy}} \int_0^{\pi/2} \int_0^{\pi/2} \int_0^{\pi/2} \int_0^{\pi/2} \\ &\mathbb{C}'_{qu}(\theta_{qx}, \theta_{qy}, \theta_{uqx}, \theta_{uqy}|\theta_{R1}) \exp\left(-\frac{(\theta_{qx} - \mu_{qx})^2}{2\sigma_{qx}}\right) \\ &\times \exp\left(-\frac{(\theta_{qy} - \mu_{qy})^2}{2\sigma_{qy}}\right) \exp\left(-\frac{(\theta_{uqx} - \mu_{uqx})^2}{2\sigma_{uqx}}\right) \\ &\times \exp\left(-\frac{(\theta_{uqy} - \mu_{uqy})^2}{2\sigma_{uqy}}\right) d\theta_{qx} d\theta_{qy} d\theta_{uqx} d\theta_{uqy}, \end{aligned} \quad (10)$$

where

$$\begin{aligned} \mathbb{C}'_{qu}(\theta_{qx}, \theta_{qy}, \theta_{uqx}, \theta_{uqy}|\theta_{R1}) &= \\ &\log(1 + \Gamma_q(\theta_{qx}, \theta_{qy}, \theta_{uqx}, \theta_{uqy}|\theta_{R1})), \end{aligned} \quad (11)$$

and $\Gamma_q(\theta_{qx}, \theta_{qy}, \theta_{uqx}, \theta_{uqy}|\theta_{R1})$ is obtained as

$$\begin{aligned} \Gamma_q(\theta_{qx}, \theta_{qy}, \theta_{uqx}, \theta_{uqy}|\theta_{R1}) &= \frac{P_{t,q}h_L(L_q(\theta_{R1}, L_{sc}, H_u))}{\sigma_n^2} \\ &\times G_0(N_{qx}, N_{qy})G_0(N_{uqx}, N_{uqy})G_e(\theta_{qx}, \theta_{qy})G_e(\theta_{uqx}, \theta_{uqy}) \\ &\times \left(\frac{\sin\left(\frac{N_{qx}(kd_{qx}\sin(\theta_{qxy})\cos(\tan^{-1}(\frac{\tan(\theta_{qy})}{\tan(\theta_{qx}})))+\beta_{qx}}{2}}\right)}{N_{qx}\sin\left(\frac{kd_{qx}\sin(\theta_{qxy})\cos(\tan^{-1}(\frac{\tan(\theta_{qy})}{\tan(\theta_{qx}})))+\beta_{qx}}{2}}\right)} \right. \\ &\times \left. \frac{\sin\left(\frac{N_{qy}(kd_{qy}\sin(\theta_{qxy})\sin(\tan^{-1}(\frac{\tan(\theta_{qy})}{\tan(\theta_{qx}})))+\beta_{qy}}{2}}\right)}{N_{qy}\sin\left(\frac{kd_{qy}\sin(\theta_{qxy})\sin(\tan^{-1}(\frac{\tan(\theta_{qy})}{\tan(\theta_{qx}})))+\beta_{qy}}{2}}\right)} \right)^2 \\ &\times \left(\frac{\sin\left(\frac{N_{uqx}(kd_{uqx}\sin(\theta_{uqxy})\cos(\tan^{-1}(\frac{\tan(\theta_{uqy})}{\tan(\theta_{uqx}})))+\beta_{uqx}}{2}}\right)}{N_{uqx}\sin\left(\frac{kd_{uqx}\sin(\theta_{uqxy})\cos(\tan^{-1}(\frac{\tan(\theta_{uqy})}{\tan(\theta_{uqx}})))+\beta_{uqx}}{2}}\right)} \right. \\ &\times \left. \frac{\sin\left(\frac{N_{uqy}(kd_{uqy}\sin(\theta_{uqxy})\sin(\tan^{-1}(\frac{\tan(\theta_{uqy})}{\tan(\theta_{uqx}})))+\beta_{uqy}}{2}}\right)}{N_{uqy}\sin\left(\frac{kd_{uqy}\sin(\theta_{uqxy})\sin(\tan^{-1}(\frac{\tan(\theta_{uqy})}{\tan(\theta_{uqx}})))+\beta_{uqy}}{2}}\right)} \right)^2 \end{aligned} \quad (12)$$

TABLE II
PARAMETER VALUES FOR SIMULATIONS.

Parameters	Values	Parameters	Values
$P_{t,s}$	1 W	$P_{t,d}$	200 mW
N_{qw}	12-18	N_{uqw}	6-18
f_c	70 GHz	$\mathbb{P}_{\text{out,tr}}$	10^{-3}
ρ_0	7.5 g/m ³	T	20°C
$\beta_{qw} = \beta_{uqw}$	0	L_{u1}	3.5 km
H_{scale}	1.5 km	L_{sd}	19 km
$\psi_{d,\text{min}}$	15°	$\psi_{s,\text{min}}$	10°
$d_{qw} = d_{uqw}$	$\lambda/2$	$\sigma_{uqx} \& \sigma_{uqy}$	1.5° & 0.5
$\sigma_{qw} \& \mu_{qw}$	0.5° & 0.3°	$\mu_{uqx} \& \mu_{uqy}$	1.7° & 1°

In (12), we have $\theta_{qxy} = \tan^{-1} \left(\sqrt{\tan^2(\theta_{qx}) + \tan^2(\theta_{qy})} \right)$, $\theta_{uqxy} = \tan^{-1} \left(\sqrt{\tan^2(\theta_{uqx}) + \tan^2(\theta_{uqy})} \right)$, and G_e is the 3GPP single element radiation pattern provided in [16]. More details about other parameters is provided in [16] and [17, Chapter 6].

Moreover, L_s and L_d are the functions of H_u , L_{sc} , and θ_{R1} as

$$\begin{aligned}
 L_s &= \sqrt{\left(L_{sc} + \frac{L_{u1}}{2} \cos(\theta_{R1}) \right)^2 + \frac{L_{u1}^2}{4} \sin^2(\theta_{R1}) + H_u^2} \\
 L_d &= \sqrt{\left(L_{dc} - \frac{L_{u1}}{2} \cos(\theta_{R1}) \right)^2 + \frac{L_{u1}^2}{4} \sin^2(\theta_{R1}) + H_u^2}.
 \end{aligned} \tag{13}$$

We consider that the NFP use the decode-and-forward (DF) relay system. Outage probability of considered system conditioned on L_s and L_d is obtained as [18]:

$$\begin{aligned}
 \mathbb{P}_{\text{out}|L_s, L_d} = \text{Prob} \left\{ \min \left[\Gamma_s(\theta_{sx}, \theta_{sy}, \theta_{usx}, \theta_{usy} | L_s, L_d), \right. \right. \\
 \left. \left. \Gamma_d(\theta_{dx}, \theta_{dy}, \theta_{udx}, \theta_{udy} | L_s, L_d) \right] < \Gamma_{\text{th}} \right\},
 \end{aligned} \tag{14}$$

where Γ_{th} is the SNR threshold.

IV. SIMULATIONS AND OPTIMAL SYSTEM DESIGN

By using Monte-Carlo simulations, we now study the optimal parameter design of the considered system. The values of the parameters used in the simulations are listed in Table II.

One of the important parameters is the optimal position for point B_p , which determines the average position of the UAV in a circular motion. As discussed, the location of point B_p is

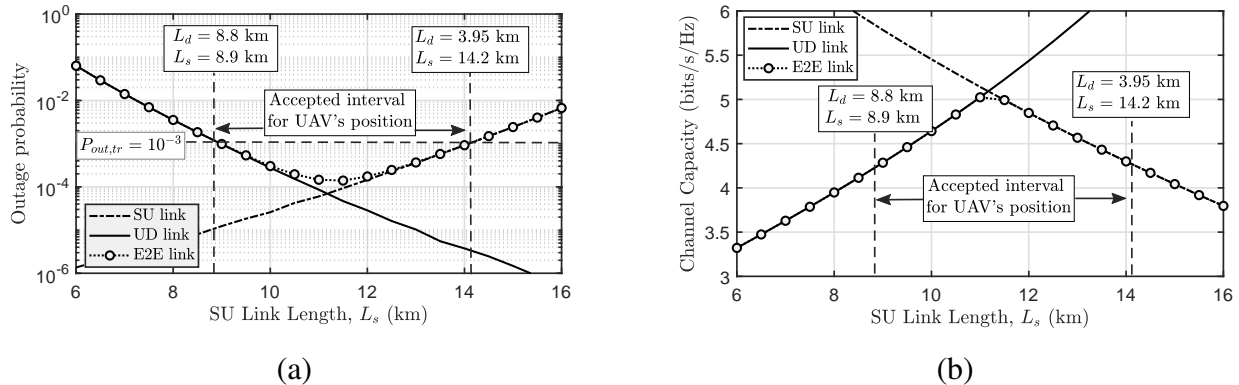


Fig. 3. E2E performance of considered system versus L_s and comparison with the the performance of CU and UR links in terms of (a) outage probability and (b) channel capacity.

adjusted in sky with the parameter L_{sc} . Any change in the parameters B_p and L_{sc} affects the values of L_s and L_d . In Fig. 3, the end-to-end (E2E) outage probability and channel capacity are plotted versus L_s for $N_{uqx} = 12$, and $N_{uqy} = N_{qw} = N_{max}$. As discussed in previous section, the E2E performance depends on the performance of CU and UR links. Therefore, in Fig. 3, to find a better view, the performance of CU and UR links are also provided versus L_s . The results obtained from the Fig. 3 can be expressed in the following two remarks.

Remark 1. For shorter links of L_s , the E2E performance can be well approximated with the performance of UR link. However, for longer links of L_s , E2E system performance is limited to the performance of SU link.

Remark 2. The optimal value for L_{sc} is very close to the length of L_s for which the capacity of SU link is equal to the capacity of UR link.

To justify **Remark 1**, note that by increasing L_s , the performance of CU link decreases and at the same time L_d decreases and consequently the performance of UR link improves. The accepted interval for L_s and L_d shown in Fig. 3a is to guarantee condition (6b). Based on (6b) and **Remark 1**, we can conclude the following remark.

Remark 3. In order to guarantee constraint (6b) along the circle flight path, it is necessary that $L_s < L_{s,max}$ and $L_d < L_{d,max}$ where $L_{s,max}$ and $L_{d,max}$ are obtained as

$$\mathbb{P}_{out,tr} = \text{Prob} \{ \Gamma_s(\theta_{sx}, \theta_{sy}, \theta_{usx}, \theta_{usy} | L_{s,max}) < \Gamma_{th} \}, \quad (15)$$

$$\mathbb{P}_{out,tr} = \text{Prob} \{ \Gamma_d(\theta_{dx}, \theta_{dy}, \theta_{udx}, \theta_{udy} | L_{d,max}) < \Gamma_{th} \}. \quad (16)$$

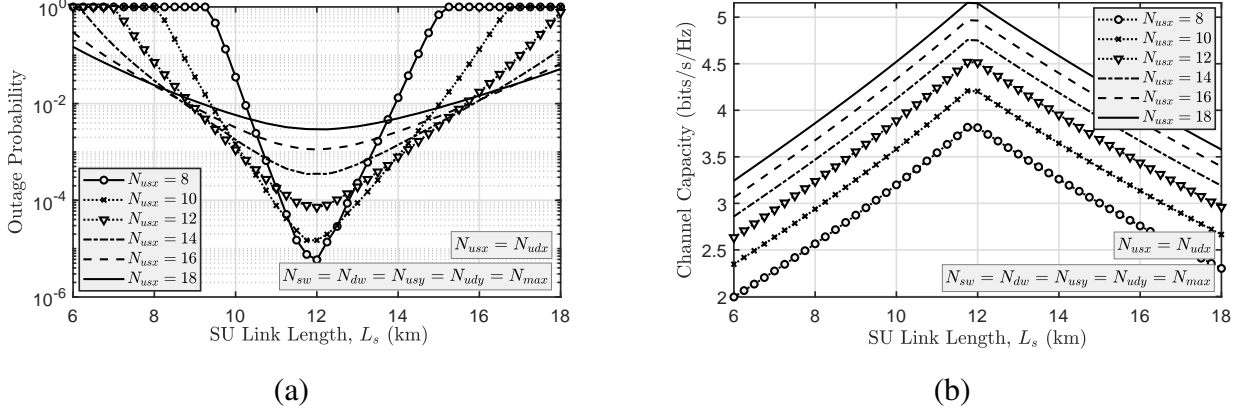


Fig. 4. E2E performance of the considered system versus L_s for different values of N_{uqx} in terms of (a) outage probability and (b) channel capacity.

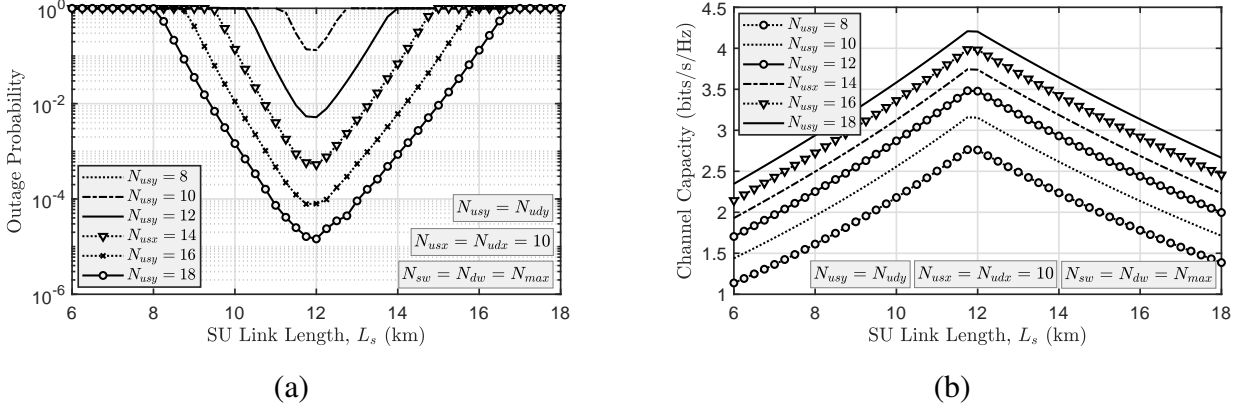


Fig. 5. E2E performance of the considered system versus L_s for different values of N_{uqy} in terms of (a) outage probability and (b) channel capacity.

Note that the parameters $L_{s,max}$ and $L_{d,max}$ are functions of the tunable parameters N_{qw} , N_{uqw} , $P_{t,q}$, frequency band, H_u , temperature, wind speed, UAV's instabilities, tracking system error, etc. In the direction of the UAV movement, the variance of antenna misalignment are higher than the variance of antenna misalignment in direction perpendicular to the UAV movement. Therefore, unlike hovering UAVs, for the considered fixed-wing UAV, we have $\sigma_{uqx} > \sigma_{uqy}$, and thus, we expect the optimal number for antenna elements to be different along the x_q and y_q axes [12]. In Figs. 4 and 5, we analyze the E2E performance of the considered system versus L_s for different values of N_{uqx} and N_{uqy} , respectively. From the results of Fig. 4, although the channel capacity gets higher by increasing N_{uqx} , the antenna beamwidth decreases for large

N_{uqx} and the system becomes more sensitive to alignment errors. Therefore, as we observe, the channel capacity is maximized for $N_{uqx} = 16$ and 18. However, for these values of N_{uqx} , we have $\mathbb{P}_{\text{out}} > \mathbb{P}_{\text{out,tr}}$ for all values of L_s and therefore, the required QoS in (6b) is not guaranteed. Therefore, it seems that the optimal value for N_{uqx} is equal to 14. However, for $N_{uqx} = 14$, the accepted interval for L_d (clearly illustrated and discussed in Fig. 3) is lower than L_{u1} and thus, the considered system cannot guarantee (6b) along the entire flight path of the UAV. As a result, for the parameter values given in Table II, the optimal value for N_{uqx} , which maximizes the channel capacity and at the same time guarantees (6b) along the entire flight path, is $N_{uqx} = 12$.

Now, in Fig. 5, the effect of N_{uqy} is investigated in the direction of y_q , which has a lower misalignment error. Unlike N_{uqx} , it is observed that with increasing N_{uqy} , the system performance in both outage probability and channel capacity improves. The reason for this is that for lower misalignment errors, the antenna is less sensitive to alignment error and an antenna with a higher gain can be used to increase the channel capacity. For the values provided in Table II, the optimal value $N_{uqy} = N_{\text{max}} = 18$. Note that in practice, due to weight and aerodynamic limitations of the UAV payload, a very large antenna cannot be used and we have to consider a maximum for N_{quw} . Based on the results of Figs. 4 and (5), we can conclude the following remark.

Remark 4. *If $\sigma_{uqy} < \sigma_{uqx}$, then the optimal value for N_{uqy} will be greater than the optimal value for N_{uqx} .*

Finding the optimal value for the system parameters is very important, especially for antenna patterns. It should be noted that the optimal values for tunable parameters will change as a result of any variations in channel parameters. For instance, UAV's instability changes due to wind speed variations which, in turn, will change the alignment error severity. Therefore, finding and updating the optimal values for the number of antenna pattern elements is vital, and the results of **Remark 4** limit the search space for discrete values of N_{uqy} and N_{uqx} , and thus, reducing the optimization time.

It is important to note that integrating on L_s to achieve the average channel capacity in the entire circular motion path of the UAV is not correct because there is not a linear relationship between flight path and L_s . In Fig. 6, the channel capacity versus θ_{R1} which is proportional to the UAV's flight, is plotted for optimal values obtained for the positions of point L_{sc} and UAV's antenna patterns. Comparing the results of Fig. 6 with the results of Figs. 4b and 5b, it is observed that the channel capacity distribution in proportion to the flight time is different from the capacity distribution relative to L_s . In order to obtain the average channel capacity and

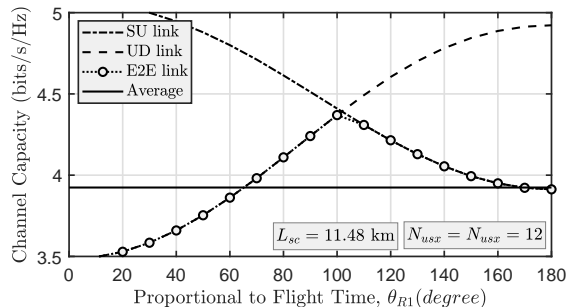


Fig. 6. Channel capacity versus UAV's flight time.

find the optimal values for antenna patterns, integration on θ_{R1} must be done. As a result, how to use the results of the figures relative to L_s and θ_{R1} is described in the following remark.

Remark 5. *To calculate the optimal UAV's flight path as well as the optimal value for L_{sc} , it is better to first investigate the performance of the considered system versus L_s since, it gives a better view in terms of finding the acceptable interval for L_s and L_d . Then, to determine the optimal antenna pattern, we need to compute channel capacity by integrating on θ_{R1} .*

V. CONCLUSION AND FUTURE ROAD MAP

In this research, taking into account the actual channel parameters such as the UAV vibrations, tracking error, real 3GPP antenna pattern, UAV's height and flight path, and considering the effect of physical obstacles, the optimal design of a relay system based on fixed wing UAV was investigated. In particular, the effects of the finding the optimal UAV's path as well as the optimal values for the number of antenna elements were studied.

Although providing closed-form expressions for the outage probability and channel capacity allows faster and more accurate analysis, this is left as future work. Therefore, it is necessary to provide analytical expressions as a function of channel parameters. For longer link lengths, two- or multi-relay systems must be used and due to the variety of tunable parameters, the design of optimal parameters is much more complicated. Due to the continuous displacement of the drone relative to CN and RA, the use of adaptive methods to control power, transmission rate and antenna pattern can be attractive. Investigating the Doppler effect according to the speed and UAV's flight rout, studying the selection of the appropriate wavelength according to the physical conditions as well as weather conditions can be important issues in this subject.

REFERENCES

- [1] M. Alzenad, M. Z. Shakir, H. Yanikomeroglu, and M.-S. Alouini, "Fso-based vertical backhaul/fronthaul framework for 5g+ wireless networks," *IEEE Communications Magazine*, vol. 56, no. 1, pp. 218–224, 2018.
- [2] W. Khawaja, I. Guvenc, D. W. Matolak, U.-C. Fiebig, and N. Schneckenberger, "A survey of air-to-ground propagation channel modeling for unmanned aerial vehicles," *IEEE Commun. Surveys Tuts.*, vol. 21, no. 3, pp. 2361–2391, May 2019.
- [3] M. T. Dabiri, H. Safi, S. Parsaeefard, and W. Saad, "Analytical channel models for millimeter wave UAV networks under hovering fluctuations," *IEEE Trans. Wireless Commun.*, Jan. 2020.
- [4] M. Banagar and H. S. Dhillon, "3D two-hop cellular networks with wireless backhauled UAVs: Modeling and fundamentals," *IEEE Trans. Wireless Commun.*, pp. 1–1, 2022.
- [5] H.-B. Jeon, S.-H. Park, J. Park, K. Huang, and C.-B. Chae, "An energy-efficient aerial backhaul system with reconfigurable intelligent surface," *IEEE Trans. Wireless Commun.*, pp. 1–1, 2022.
- [6] M. Gapeyenko, V. Petrov, D. Moltchanov, S. Andreev, N. Himayat, and Y. Koucheryavy, "Flexible and reliable UAV-assisted backhaul operation in 5G mmWave cellular networks," *IEEE J. Sel. Areas Commun.*, vol. 36, no. 11, pp. 2486–2496, 2018.
- [7] B. Galkin, J. Kibilda, and L. A. DaSilva, "Backhaul for low-altitude UAVs in urban environments," in *Proc. IEEE International Conference on Communications (ICC), Kansas City, MO, USA*, May 2018.
- [8] N. Tafintsev, D. Moltchanov, M. Gerasimenko, M. Gapeyenko, J. Zhu, S.-p. Yeh, N. Himayat, S. Andreev, Y. Koucheryavy, and M. Valkama, "Aerial access and backhaul in mmWave B5G systems: Performance dynamics and optimization," *IEEE Commun. Mag.*, vol. 58, no. 2, pp. 93–99, 2020.
- [9] W. Wang, N. Cheng, Y. Liu, H. Zhou, X. Lin, and X. Shen, "Content delivery analysis in cellular networks with aerial caching and mmWave backhaul," *IEEE Trans. Veh. Technol.*, vol. 70, no. 5, pp. 4809–4822, 2021.
- [10] C. T. Cicek, H. Gultekin, B. Tavli, and H. Yanikomeroglu, "Backhaul-aware optimization of UAV base station location and bandwidth allocation for profit maximization," *IEEE Access*, vol. 8, pp. 154 573–154 588, 2020.
- [11] Z. Feng, L. Ji, Q. Zhang, and W. Li, "Spectrum management for mmwave enabled UAV swarm networks: Challenges and opportunities," *IEEE Commun. Mag.*, vol. 57, no. 1, pp. 146–153, 2018.
- [12] M. T. Dabiri, M. Rezaee, V. Yazdaniyan, B. Maham, W. Saad, and C. S. Hong, "3D channel characterization and performance analysis of UAV-assisted millimeter wave links," *IEEE Trans. Wireless Commun.*, vol. 20, no. 1, pp. 110–125, 2020.
- [13] Y. Yu, X. Bu, K. Yang, H. Yang, and Z. Han, "UAV-aided low latency mobile edge computing with mmWave backhaul," in *ICC 2019-2019 IEEE International Conference on Communications (ICC)*. IEEE, 2019, pp. 1–7.
- [14] M. T. Dabiri, S. M. S. Sadough, and M. A. Khalighi, "Channel modeling and parameter optimization for hovering UAV-based free-space optical links," *IEEE J. Sel. Areas Commun.*, vol. 36, no. 9, pp. 2104–2113, 2018.
- [15] "Attenuation by atmospheric gases," Recommendation ITU-R P.676-3.
- [16] 3GPP TR 37.840 v12.1.0, "Technical specification group radio access network; study of radio frequency (RF) and electromagnetic compatibility (EMC) requirements for active antenna array system (AAS) base station," *Tech. Rep.*, 2013.
- [17] C. A. Balanis, *Antenna theory: analysis and design*. John wiley & sons, 2016.
- [18] M. O. Hasna and M.-S. Alouini, "Outage probability of multihop transmission over Nakagami fading channels," *IEEE Commun. Lett.*, vol. 7, no. 5, pp. 216–218, 2003.